nature synthesis

Article

https://doi.org/10.1038/s44160-025-00931-3

Synthesizing high-entropy alloy materials and coatings using a bilayer ice recrystallization method

Received: 18 February 2025

Accepted: 13 October 2025

Published online: 11 November 2025

Check for updates

Kaiqi Li[1,5], Xiaoyue Sun[1,5], Qikai Wu[2,5], Chuanbiao Zhang[3,5], Dan Wang[1], Shuai Guo[4], Xiaofei Chen[1], Xiaoting Chen[1], Tianding Xu[2], Ran Du[1] ✉, Yao Yang[2] ✉ & Zhiyuan He[1] ✉

High-entropy alloys (HEAs) are usually synthesized by stabilizing thermodynamically metastable structures from high temperatures. Here we present a bilayer ice recrystallization approach performed at subzero temperatures to synthesize HEA nanoparticles or aerogels with up to 11 metal elements. We found that, below 0 °C, premelted ice channels can regulate the uniform emission of metal salts and reductants to form HEA seeds. The seeds function as anti-icing agents akin to antifreeze proteins, promoting uniform element mixing and assembly at ice grain boundaries to form HEA nanoparticles or HEA aerogels. In addition, by introducing an arbitrary template, we synthesized nanometre-thick uniform HEA coatings on diverse metal or alloy nanoparticles and macroscale aerogels. The bilayer ice recrystallization method demonstrates the application of ice chemistry for the synthesis of high-entropy-based materials with hierarchical architectures.

High-entropy alloys (HEAs) attract attention due to the expansion of material libraries by uniform mixing of multiple immiscible principal elements, which enhances configurational entropy, stabilizes single-phase solid solutions, and enables tuneable mechanical, thermal and chemical properties[1–5]. However, the synthesis of HEA nanoparticles (HEA-NPs) is difficult, as most metal elements remain immiscible at mild temperatures during traditional wet-chemical methods. In aqueous solutions, the characteristic micromixing time of reactants (approximately ~5–50 ms) is larger than the nucleation induction time (approximately 1 ms or less), leading to inefficient mixing of reactants and non-uniform element distribution in the resulting NPs[6–9]. Pyrolysis-based methods have been introduced to mix different elements in the gas or liquid phases at high temperatures where thermodynamically stable, then quenching to limit atom diffusion and form single phase, but extreme conditions are required[10–13]. Hot injection or liquid gallium metal synthetic routes can achieve milder reaction conditions but are limited to certain systems or multiple reaction steps are needed[14–16]. Moreover, previous methods usually need supporting substrates or capping ligands to avoid structure coarsening under high temperatures, which incurs additional post-treatment steps and impedes the synthesis of multilevel structures.

Ice is an abundant matter on Earth with crucial roles in our environments and human activities[17–19]. Chemical reactions in ice can be controlled precisely and differently from liquid phase reactions since below 0 °C, there will be a thin premelted layer on the surface, which forms a natural reactor with interesting kinematics and thermodynamics[20–24]. Ice-based chemistry, including mediated reactions and assembling processes, has been applied in aerogels and nano composites[25–36]. Here, we report a bilayer ice recrystallization (BLIR) strategy capable of structuring diverse HEA-NPs and three-dimensional centimetre-sized

[1]School of Materials Science and Engineering, Beijing Institute of Technology, Beijing, China. [2]Department of Materials Science and Engineering, Westlake University, Hangzhou, China. [3]College of Physics and Electronic Engineering, Heze University, Heze, China. [4]Department of Applied Physics, The Hong Kong Polytechnic University, Hong Kong, China. [5]These authors contributed equally: Kaiqi Li, Xiaoyue Sun, Qikai Wu, Chuanbiao Zhang. ✉e-mail: rdu@bit.edu.cn; yangyao@westlake.edu.cn; hezy@bit.edu.cn

https://doi.org/10.1038/s44160-025-00931-3

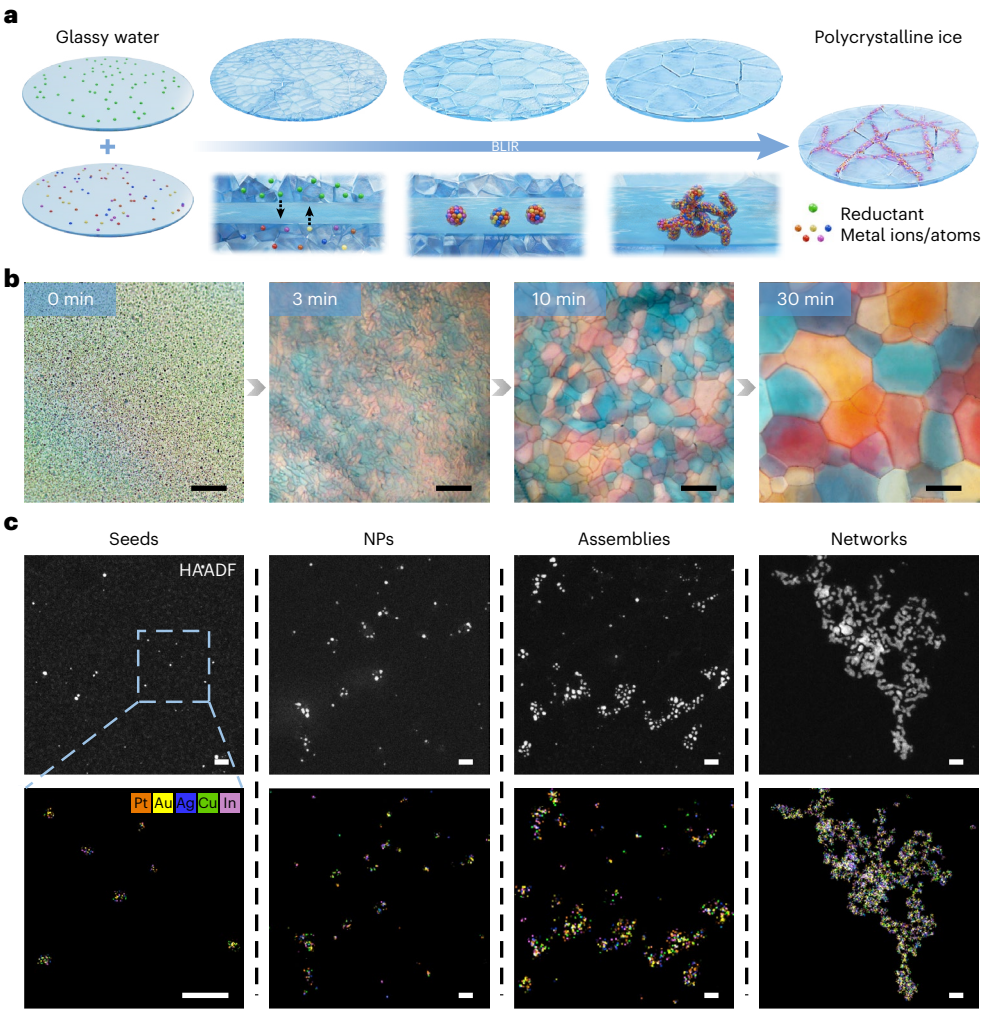

Fig. 1 | Synthesis of HEA-NPs and HEAAs by the BLIR strategy. a, A scheme of the BLIR based synthesis process on HEA-NPs and HEAAs. **b**, Representative images of ice recrystallization by polarized optical microscopy. Scale bars, 100 µm. **c**, Cryogenic HAADF-STEM images and corresponding EDX maps of PtAuAgCuIn HEAAs system prepared by the BLIR method during ice recrystallization. Scale bars, 10 nm.

HEA aerogels (HEAAs) consisting of up to 11 immiscible metals with uniform and tuneable element distributions. During the recrystallization of the two flashing-frozen vitreous ice layers, premelted ice will only enable limited emission and diffusion of reductants and metal ions. This achieves uniform element mixing at the atomic level and thus yields HEA-NPs, shown to be thermodynamically stable by simulation. The aggregation behaviour of formed HEA seeds was then probed by single ice crystal growth experiments. We found HEA seeds will steadily aggregate at the interfaces of ice grain boundaries and grow into NPs, which perform similar to the anti-icing agents, evolving into gels. These HEA gel networks will finally form the HEAAs through freeze-drying. In addition, by performing BLIR on as-formed nanoarchitectures with leveraged reaction sequences of different metal precursors, HEA coatings (HEACs) are successfully fabricated on tuneable templates including metal or alloy NPs and macroscopic aerogels.

Results and discussion

Synthesis of HEA-NPs and HEAAs by BLIR

The BLIR process happens at subzero temperatures, where ice recrystallization-regulated solute diffusion governs the reaction kinetics at the atomic scale and directs the assembly of various metal sources (Fig. 1a and Extended Data Fig. 1). The solutions of mixed metal salts and reductants, respectively, were hyperquenched first on a substrate held at 77 K by a two-step splat cooling technique, which is a common method to make thin layer amorphous ice (named vitreous ice or glassy water) compared with bulk from the fast-quenching method in cryo-transmission electron microscopy[37–39]. At this temperature, there is no premelted ice layer between the mixed metal salts layer and the reductants layer[24]. To generate the premelted ice channel among ice and activate the recrystallization, we anneal the glassy water at higher temperatures (named T_r). Metal salts and reductants would indiscriminately, uniformly and continuously diffuse and react within the premelted ice channels between recrystallized ice grains. Because of the delayed diffusion and reduction process and thermal perturbation at subzero temperatures[40,41], HEA-NPs with uniformly distributed elements would gradually form. When the ice recrystallization continues, the smaller ice grains merge with each other and become larger, pushing the movement of grain boundaries to further release metal ions and reductants, which also provides a platform for NP assembly. Driven by the high surface energy and the freezing-induced concentration[42,43], NPs would steadily contact and fuse into multiscale assemblies without altering the even element distribution. The entire process reflects coupling of recrystallization dynamics and solute transport in bilayer ice systems. When the reaction happens at room temperature, the emission rate of reductants and different metal ions cannot be accurately controlled, the gel will perform as a separated phase (Supplementary Fig. 1).

To monitor the ice recrystallization process, polarized optical microscopy, high-angle annular dark-field scanning transmission

electron microscopy (HAADF-STEM) and energy-dispersive X-ray spectroscopy (EDX) were performed on the PtAuAgCuIn system (Methods; Fig. 1b,c). At the beginning, the glassy water clearly shows the amorphous state while the HAADF-STEM and EDX images show the uniform distribution of metal salt seeds. When annealing at a higher temperature, the glassy water started to recrystallize and form small grains with an average size of 31.1 ± 4.4 μm. Between the two ice layers, uniform amount of metal ions with different species were reduced to form NPs of uniform metal atoms (Supplementary Figs. 2 and 3). As the annealing continues, the ice grains became larger (around 129.0 ± 18.9 μm), and NPs started to assemble and form aggregates (Supplementary Fig. 4). Finally, the grains enlarged to 159.8 ± 19.0 μm, and the ice-mediated assembly process was completed.

By systematically investigating the kinetics of ice recrystallization, we optimized the processing conditions and successfully synthesized a quinary HEAA (Methods; Extended Data Figs. 2a and 3 and Supplementary Fig. 5). It not only enables us to identify various stages of nanoarchitectures during the BLIR process but also allows us to synthesize HEAs with different forms (NPs, aggregates and aerogels), which can be used in different areas such as catalysis[44–46], energy storage[47,48] and bioapplication[49,50] by simply controlling the reaction time. The stability and electrochemistry tests of the as-synthesized HEAA further confirmed its potential for practical applications (Methods; Supplementary Figs. 6 and 7).

Following the precise programming of the BLIR process, we have synthesized not only quinary but also septenary, novenary and undecimal HEA-NPs and HEAAs, incorporating various combinations of elements from both noble and non-noble groups (Fig. 2a, Extended Data Figs. 2b–d and 4 and Supplementary Figs. 8–11). The atomic radius ranges from 1.24 to 1.67 Å, spanning from transition metals to noble metals, showing the flexibility of element mixing (Supplementary Table 1). All the free-standing HEAAs synthesized by thawing and freeze-drying the gel solution can reach up to centimetre-level diameter and have highly porous structures with large specific surface areas (Supplementary Fig. 12 and Supplementary Tables 2 and 3). We examine undenary PtAuAgCuInPdRhRuCoBiNi HEAA, the density of which is 61.8 ± 3.6 mg cm^{-3}. This is smaller than 0.4 wt% of the density of usual bulk metal, which enables aerogels to stand on the petals of a flower (Fig. 2a). The X-ray diffraction (XRD) patterns suggest all HEAAs manifest a single-phase fcc structure, while the lattice spacing differs because of the lattice distortion incurred by the size difference of dissimilar metal atoms[51] (Fig. 2b). When zooming in from macroscopic HEAA materials to microscopic view, we can see that the ligaments of synthesized HEAAs have nanometre thickness, and the element distributed uniformly with component fractions ranging from 5% to 35% (Fig. 2c,d and Supplementary Tables 2–4).

Mechanism of atomic mixing and macroscopic assembly of HEAAs

To disclose the ice-mediated formation mechanism of HEAAs with uniformly distributed elements at the atomic level, molecular dynamics simulations were performed (Methods; Fig. 3a and Extended Data Fig. 5). Taking a quinary metallic system (PtAuAgCuNi) as an example, premelted ice channels between ice grains serve as the reaction place. Uniform amount of metal ions with different species were reduced to atoms by the limited supply of premelted ice solution. With the advancement of the ice front over time, different kinds of metal atoms assembled into small clusters, which gradually grow larger, ultimately forming multicomponent alloy clusters, featuring the entropy of mixing (ΔS_{mix}) approaching the theoretical high-entropy limit (1.61R, where R is the ideal gas constant). Figure 3b shows the entire process can be broadly divided into three regions: (1) during the initial phase, the rapid formation of HEA-NPs enables ΔS_{mix} to quickly approach the ideal mixing entropy (ΔS_{ideal}), although the number of ice molecules (N_{ice}) and the size of assemblies are still evolving. (2) As the ice front advances, the ice-mediated assembly process unfolds, resulting in the formation of larger assemblies accompanied by an increase in the N_{ice}. (3) In the final phase, all NPs within the system undergo coalescence, forming a stable assembly that marks the completion of the ice-mediated process. We then calculated the Warren–Cowley parameter (WCP) to quantitatively evaluate the chemical short-range order between different pairs of elements and the extent of nanophase separation, as ΔS_{mix} only reflects the average effect of the whole system[52]. Figure 3c and Supplementary Fig. 13 show that the values of WCP between different metal elements approach zero, indicating scarce phase separation and uniform element distribution in the quinary HEAAs. The size of assembled HEA clusters increases with ice recrystallization temperature (Supplementary Fig. 14). The freeze-concentration effect during recrystallization leads to elevated solute concentrations within premelted water channels. Within a defined concentration range, HEA cluster formation remains consistent regardless of initial solute concentration (Supplementary Fig. 15). Simulations using different water models (TIP4P/Ice[53] and mW[54]), metal potentials (Lennard–Jones (LJ) and embedded atom method[55]) and varied water–metal interaction potentials consistently produced HEA clusters, indicating that the simulation results are insensitive to the water models and metal force fields (Supplementary Figs. 16 and 17). This process provided a microscopic perspective on the construction of ice-mediated HEAAs, aligning with the experimental observations.

We then investigated the interaction between NPs and the ice–water interface to understand the assembly of macroscopic HEAAs. The ice surface interacts with NPs in three different ways: NPs can be engulfed in ice, rejected into premelted ice channels, and adhered to the ice surface[56]. Single ice crystal growth experiments, routinely conducted to evaluate the interaction between antifreeze proteins and ice, provide a powerful means to investigate the interaction mechanisms between NPs and ice[57] (Methods and Supplementary Fig. 18). Notably, only the ice-binding materials that can effectively attach onto the ice surface exhibit the typical shaping effect of a single ice crystal[58]. Equivalent properties were found in HEA-NP systems. As shown in Fig. 3d and Extended Data Fig. 6, we studied the growth processes of single ice crystals in pure water and diverse NP sols. In stark contrast with the disc-shaped ice crystal in pure water, the growth rate of ice was considerably delayed and apparent hexagonally shaped ice crystals were captured in multimetallic sols. These signalled the enrichment of HEA-NPs on the prism plane of ice, thus shaping the ice crystal and inhibiting ice growth as previously found in the antifreeze protein contained systems[59,60] (Supplementary Fig. 19). The enrichment and assembly of fluorescently labelled HEA-NPs at a moving ice front were also confirmed by in situ cryogenic laser confocal microscopy (Supplementary Figs. 20–22).

In addition, the microscopic pictures of these findings are rationalized as schemed in Fig. 3e. Once the moving ice front attaches HEA-NPs, the NPs lead to micro-curvatures on the ice surface, thus inhibiting the ice recrystallization process and establishing a stable ice–NP interface. Hydrophobic interactions facilitate the continuous aggregation of HEA-NPs at the ice surface. Hence, the ice surface can offer a stable two-dimensional interface for attachment and assembly, facilitating the formation of HEAAs, similar to the adsorption-assembly mechanism[57]. Notably, because the assembly process is achieved in a low-temperature and confined environment, thermal motion is largely retarded. In this light, HEA-NPs can evolve into gels steadily with minimized migration and rearrangement of metal atoms, maintaining the uniform element distribution.

Synthesising nanometre-thick HEACs

The BLIR programme can precisely control each step of assembly of the macroscopic HEAAs with uniform element mixing at the atomic level. By introducing existing structures to the ice at the beginning and controlling the kinetics, we can further utilize the ice-mediated strategy to yield

https://doi.org/10.1038/s44160-025-00931-3

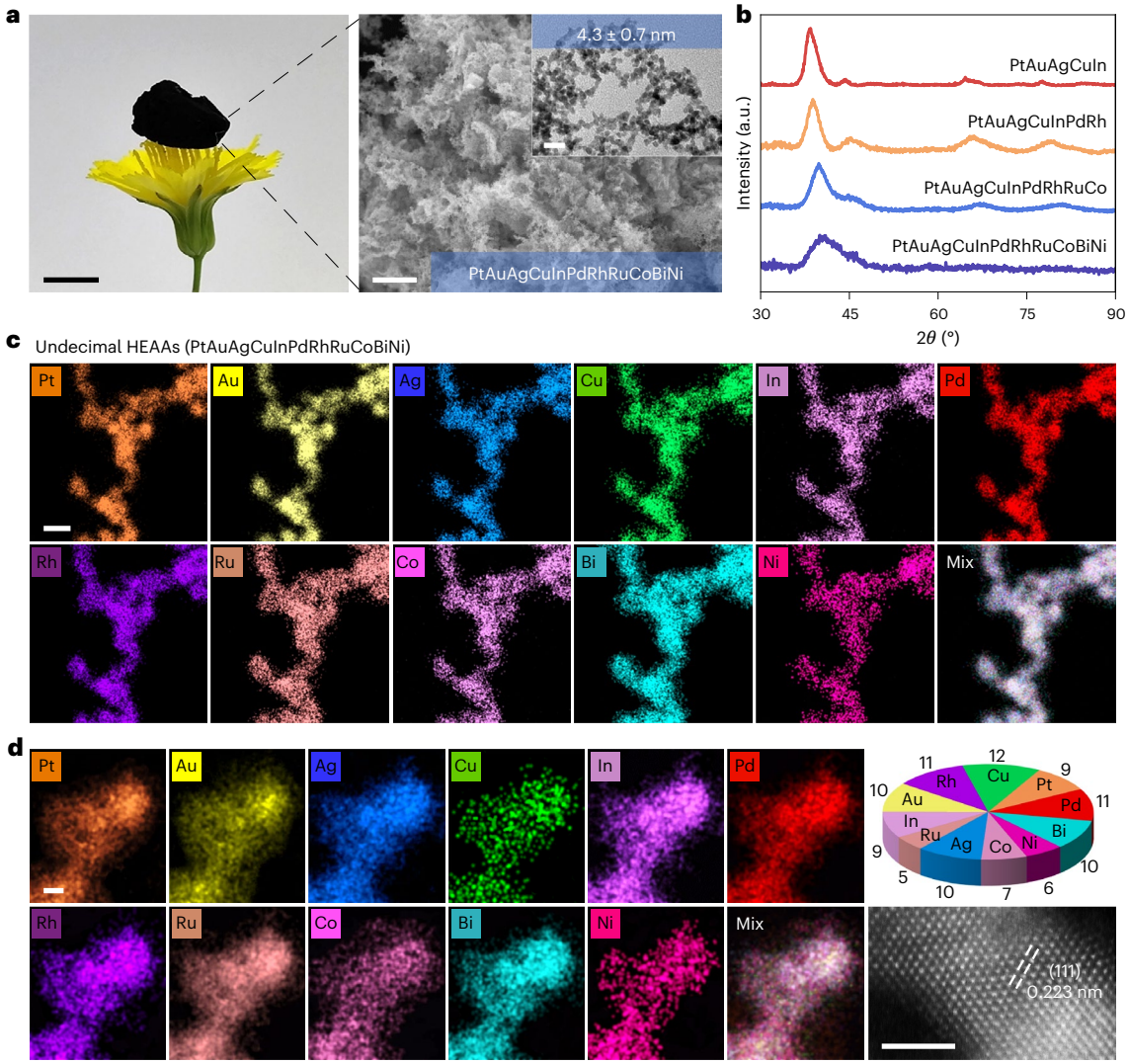

Fig. 2 | Characterization of HEAAs. a, A photograph of a self-supported undecimal PtAuAgCuInPdRhRuCoBiNi aerogel on the *Ixeridium sonchifolium* (Maxim.) Shih. Scale bar, 1 cm. SEM image and TEM image (inset) of the corresponding aerogel. Scale bar (SEM image), 1 µm; scale bar (TEM image), 20 nm. **b**, XRD patterns of diverse HEAAs. **c**, Low magnification EDX maps of the undecimal PtAuAgCuInPdRhRuCoBiNi aerogel, the ligament size is 4.3 ± 0.7 nm. Scale bar, 20 nm. **d**, High magnification EDX maps, composition ratio and HR-STEM image of the undecimal PtAuAgCuInPdRhRuCoBiNi aerogel. Scale bar, 2 nm.

more complex structures by heterogeneous nucleation (Methods). Taking Au-based systems as examples, as schemed in Fig. 4a, after the first-run recrystallization to create the Au network, a third ice layer containing multiple metal sources was introduced by a similar splat cooling technique before conducting the second-run recrystallization. Driven by the lower energy barrier compared with homogeneous nucleation, subsequent metals preferentially nucleate and grow conformally on the pre-formed Au gels. Following this mechanism, a HEA-coated Au aerogel was synthesized. The Au@PtAgCuInPdRhRuCoBiNi aerogel also preserved the self-standing property of the aerogels, which is the same as HEAAs (Fig. 4b and Supplementary Table 2). But unlike HEAAs, the XRD pattern shows two distinct sets of peaks: one set of diffraction peaks from the Au core and another set, identified by a lattice fringe of 0.224 nm corresponding to the (111) peak of the HEA shell, showing the distinct core–shell features.

By controlling the forms of existing structures to the ice and the steps of the assembly during BLIR process, we were able to obtain various nanoarchitectures, such as HEA-coated NPs and HEA-coated networks (Fig. 4c–f and Supplementary Figs. 23 and 24). HR-STEM images and EDX maps revealed a well-defined core–shell structure in a Au@PtAgCuInPdRhRuCoBiNi NP by atomic contrast and spectroscopic information. The HEAC was composed of ten uniformly distributed elements with around 1 nm, which have not been achieved by any other methods before (Fig. 4d). When elongating the assembly time, HEA-coated Au aerogels were acquired, where the lattice spacings distinct from the Au core (0.235 nm) to the HEA shell (0.225 nm), which is aligned with the XRD pattern (Fig. 4e,f and Extended Data Fig. 7). To further identify the spatial distribution of different elements in the coated aerogel, a fused multimodal electron tomography experiment was conducted on one nanotube of the Au@PtAgCuInPdRhRuCoBiNi core–shell HEA-coated aerogel[61]. Combining the annular dark-field (ADF) and spectroscopy modes in HR-STEM, ADF projections and EDX projections were acquired at different tilted angles from the core–shell HEA aerogel (Extended Data Fig. 8 and Supplementary Fig. 25). The combined tilt series were then reconstructed by a fused multimodel tomographic method with gradient descent algorithm on the loss functions of atomic contrast and element consistency to save the dose and improve the signal-to-noise ratio (Methods). The fused tomography of different elements in the HEA shell along with the Au core presents a uniform distribution (Fig. 4g). The line profile of the fused tomogram shows a sharp boundary between the Au core and HEA shell, meaning that no element exchange happens during the HEAC

https://doi.org/10.1038/s44160-025-00931-3

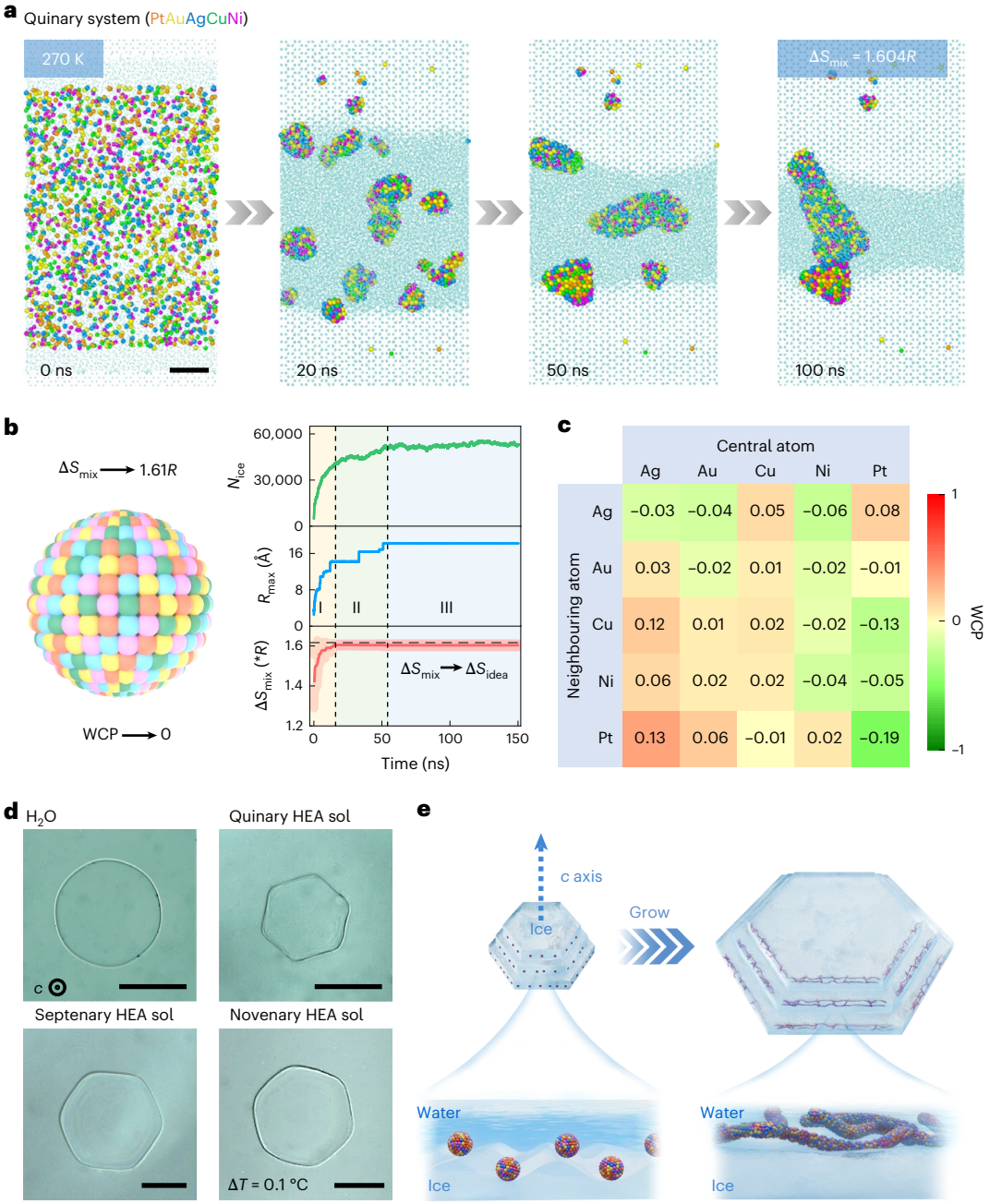

Fig. 3 | Formation and assembly mechanism of HEA-NPs and HEAAs. **a**, Snapshots of the molecular dynamics simulations for the evolution process of a quinary metallic system. Scale bar, 2 nm. **b**, The entropy of mixing (ΔS_{mix}) and WCP of the quinary metal NPs with idealized homogeneously distributed elements. The number of ice molecules (N_{ice}), the radius of the max NP and the average ΔS_{mix} of the three largest NPs versus time. **c**, The WCP matrix for the resulting quinary NPs. **d**, Optical images of single ice crystal growing in pure water and diverse NP sol under $\Delta T = 0.1$ °C. The concentration of the quinary NP sol is 0.2 mM. Quinary HEA: PtAuAgCuIn; septenary HEA: PtAuAgCuInPdRhM; novenary HEA: PtAuAgCuInPdRhRuCo. Scale bars, 100 μm. **e**, A schematic illustration of the assembly process of quinary NPs at ice–water interfaces.

fabrication (Supplementary Fig. 26), which is also an advantage of low-temperature synthesis.

Based on the feasibility and precision of the BLIR process, the synthesis strategy can also be expanded to create other HEA-coated aerogels. We have synthesized HEA-coated metal aerogel with different metal cores and different types of element in HEAC, such as Ag@PtAuCuInPdRhRuCoBiNi and Cu@PtPdAgRhNi (Extended Data Figs. 9 and 10a). Moreover, we also successfully achieved HEA-coated bimetallic alloy aerogels, such as AuCu@PtPdAgRhNi (Extended Data Fig. 10b). These unique nanoarchitectures, which cannot be achieved by other strategies reported so far, may not only reduce the amount of high-cost HEA but also offer opportunities to finely tune the strain and thus the electronic structure of HEA shell by designing the composition/crystalline structure of core metal/alloy[62,63].

Conclusion

In summary, we demonstrated a BLIR strategy that yields multiscale structured HEAs at subzero temperatures, at the atomic scale. By spatiotemporally manipulating the ice recrystallization process, we have efficiently controlled the release, diffusion, reaction and assembly behaviours of different metal species, methodically achieving tailored HEA-NPs and HEAAs, respectively. Intentionally introducing a third layer further yielded

https://doi.org/10.1038/s44160-025-00931-3

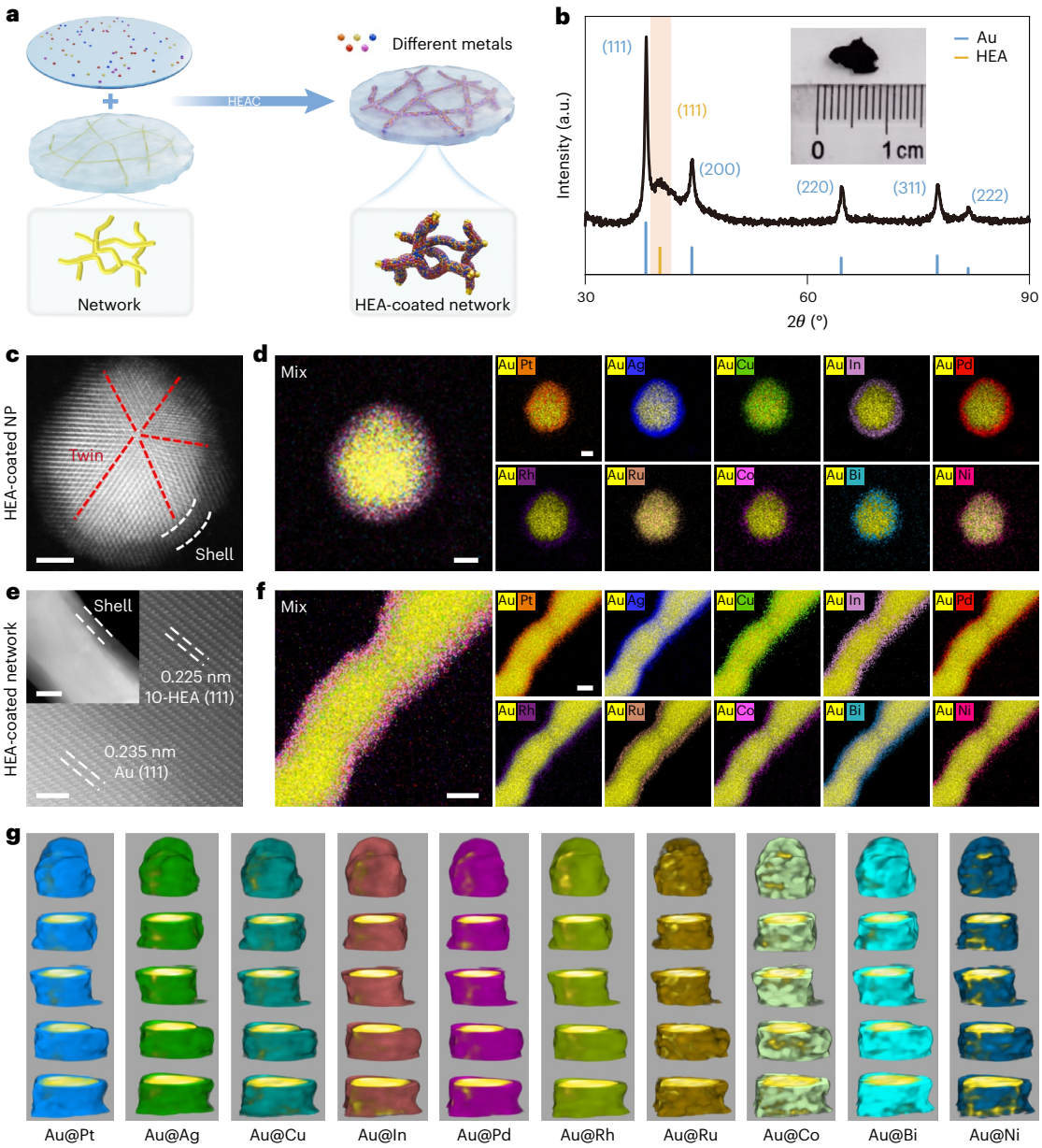

Fig. 4 | Nanometre-thick HEA-coated NPs and aerogels. a, The fabrication process of the HEAC on metal/alloy aerogels. **b**, The XRD patterns of Au@PtAgCuInPdRhRuCoBiNi aerogel and photograph (inset) of corresponding aerogel. **c**,**d**, HR-STEM image (**c**) and EDX maps (**d**) of the Au@PtAgCuInPdRhRuCoBiNi NP. Scale bars, 2 nm. **e**, HR-STEM image of HEA-coated network showing the lattice differences of Au core and HEA shell. Scale bar 1 nm. Scale bar (inset STEM image), 20 nm. **f**, EDX maps of HEA-coated network. Scale bars, 10 nm. **g**, Fused multimodal tomogram of the Au@PtAgCuInPdRhRuCoBiNi aerogel, different subimages represent Au core with different elements in HEAC, showing the uniformity.

a variety of HEACs on metal or alloy NPs and aerogels that are unattainable by other strategies, highlighting the uniqueness and effectiveness of the ice-based chemistry method. Compared with the conventional HEA fabrication approaches, our method reduces the operating temperature and offers opportunities to synthesize macroscopic materials with designable, complicated and preserved multilevel nanostructures. It is envisioned this ice-mediated strategy can expand to develop diverse high-entropy materials (for example, oxides, sulphides, layered double hydroxides and perovskites) and other metal and non-metal materials with desired element distributions and tailored functions.

Methods

Synthesis of HEA-NPs and aerogels

The recrystallization of flashing-frozen ice was recently confirmed to offer strong controllability for tuning the ice–matter interactions due to the retarded thermal perturbation at subzero temperatures[40,41]. Using PtAuAgCuIn system as an example, a solution (5 ml) of metal salts (K_2PtCl_4, $HAuCl_4$, $AgNO_3$, $CuCl_2$ and $In(NO_3)_3{\cdot}xH_2O$, 0.2 mM for each) was dropped from a height of 1 metre onto a precooled Petri dish (Extended Data Fig. 1), creating the initial ice layer. Then a freshly prepared $NaBH_4$ aqueous solution (2 mM, 5 ml) was poured to form a second ice layer. The bilayer ice was annealed at 243 K to perform recrystallization for 5 minutes to grow HEA-NPs. To isolate them, a surfactant such as hexadecyltrimethylammonium bromide was used. If not using surfactants and annealing at 243 K for 60 min, the NPs will be naturally connected and from microgels. The iced microgels could then be thawed and grounded for 8 h at room temperature to yield the hydrogel. After purification and solvent exchange with tert-butanol, the resulting wet gel was freeze-dried to yield an aerogel.

Synthesis of HEA-coated NPs and aerogels

Here, we use Au@PtAgCuInPdRhRuCoBiNi as an example. After the formation of Au-based NPs or gel by using the described BLIR method, a third layer was prepared on it by splat cooling with an aqueous solution of metal salts containing equimolar $AgNO_3$, K_2PdCl_4, K_2PtCl_4, $RuCl_3$, $CuCl_2$, $NiCl_2{\cdot}6H_2O$, $(NH_4)_3RhCl_6$, $BiCl_3$, $In(NO_3)_3{\cdot}xH_2O$ and $CoCl_2{\cdot}6H_2O$. After undergoing a two-stage annealing process at 243 K for 1 h followed by 263 K for 1 h, the sample was then thawed. The HEA-coated aerogel was created after freeze-drying.

XRD and inductively coupled plasma optical emission spectroscopy characterizations

XRD was carried out in reflection mode using a D8 Advance instrument (AXS-Bruker) equipped with Cu Kα radiation. The data were collected in the range of 30–90° (2θ) with a step size of $\Delta 2\theta = 0.02°$. Inductively coupled plasma optical emission spectroscopy was performed on a Prodigy 7 optical emission spectrometer (Leeman Labs).

Microscopy characterization

Scanning electron microscopy (SEM) images were captured with a Zeiss Gemini 500 microscope, where the aerogels were directly adhered to conductive tapes. Transmission electron microscopy (TEM), high-resolution TEM (HR-TEM), HAADF-STEM imaging and EDX based spectroscopic imaging were conducted by using a JEM-2100F microscope. This microscope is operated at 200 kV and is equipped with an X-FEG electron source and a Super-X EDX detector system. Spherical aberration-corrected TEM was characterized by FEI Themis Z operated at 300 kV. Before analysis, the specimen mounted in a high-visibility, low-background holder was placed for 10 s into a Model 1020 Plasma Cleaner (Fischione) to remove possible contamination. Thermo Fisher Scientific Spectra Ultra S/TEM is equipped with a new generation Ultra-X EDX detector that can accommodate a 4.04 srad solid angle with an analytical double tilt holder. For ex situ TEM observations, the sample was prepared on a grid, ripened for different times using a cryo-stage (Instec), then quenched and freeze-dried. Polarized optical microscopy images were collected by using a Nikon optical microscope (LV100ND, Japan) equipped with a digital camera (Nikon Y-TV55, Japan).

Ice recrystallization analysis

Ice recrystallization was performed via the splat cooling method. The experimental apparatus was composed of a Nikon optical microscope (LV100ND, Japan) equipped with a digital camera (Nikon Y-TV55, Japan) and an Instec cryo-stage. The experimental procedure is described as follows: a 10 µl droplet of HEA sol was dropped onto the cover glass precooled to 123 K from a height of 1 metre, forming a piece of amorphous ice. The temperature was then increased to the target value (ranging from 213 to 268 K), and the samples were annealed at the target temperature for 120 min, with images acquired at specified intervals. For each figure, the sizes of the 25 largest grains were measured using ImageJ to calculate the mean grain size.

Electrochemical measurements

The catalyst ink was dispersed 1.0 mg as-synthesized metal aerogels or Pt/C (20 wt%, supported on Vulcan XC-72 black, Johnson Matthey) in a mixture of isopropanol (990 µl) and Nafion dispersion (5 wt%, 10 µl). The suspension was ultrasonicated for over 2 h in an ice bath. After sonication, the ink was dropped onto a glassy carbon rotating disk electrode (5 mm diameter) and allowed to dry in the air.

Electrochemical tests were performed on an electrochemical workstation (Metrohm Autolab PGSTAT302N) with a catalyst-coated glassy carbon electrode mounted on a rotator (Pine Instruments) as the working electrode. All glassware was cleaned in an acidic solution of potassium permanganate overnight, followed by rinsing with an acidic solution of hydrogen peroxide, repetitive rinsing and boiling with ultrapure water. A coiled platinum wire served as the counter electrode, and a reversible hydrogen electrode (RHE, Mini HydroFlex, Gaskatel) was employed as the reference electrode. All potentials are reported versus RHE.

The accelerated durability test was performed at 298 K in 0.1 M $HClO_4$ solutions by applying the cyclic potential sweeps between 0.6 and 1.1 V versus RHE at a sweep rate of 100 mV s^{-1}.

Gas adsorption measurement

Nitrogen adsorption experiments were performed with a Micromeritics ASAP 2020 system at 77 K. All samples were degassed at 323 K for ~24 h under vacuum before measurement. The filling rod was used to reduce the dead volume and improve the measurement accuracy. The specific surface area was calculated by using the multipoint Brunauer–Emmett–Teller equation ($0.1 < p/p_o < 0.3$). The pore size distribution was derived by using the non-local density functional theory method. The total pore volume was calculated at $p/p_o = 0.99$.

Molecular dynamics simulations

The molecular dynamics simulations were performed by LAMMPS[64]. Water was modelled with the mW water model, which has been widely validated for the study of the structure, interfacial properties and thermodynamics of water and ice[54]. The interactions among metal atoms and between oxygen atoms in water molecules and metal atoms were described by the LJ potential where the Lorentz–Berthelot combining rule is adopted[65]. For σ and ε between oxygen atoms in water molecules and metal atoms, $\sigma_{MO} = \frac{\sigma_M + \sigma_O}{2}$ and $\varepsilon_{MO} = \alpha\sqrt{\varepsilon_M \varepsilon_O}$, where M represents metal atoms, O represents oxygen atoms and α is adopted to give a reasonable description of the water–metal contact angle[66,67]. The LJ parameters for water–metal interactions are provided in Supplementary Table 5. At the beginning of the simulation, two hexagonal ice (I_h) slabs were positioned at the top and bottom of the simulation box. The exposed surface of the ice slab along the z axis corresponds to the secondary prismatic plane. The ice structures were generated using the GenIce program[68]. Periodic boundary conditions were applied in all three directions during the simulations. The simulation box has dimensions of $10.9 \times 10.2 \times 20.0$ nm^3 and contains a total of 69,953 water molecules and 2,000 metal atoms, comprising five species (Ag, Au, Cu, Ni and Pt) with 400 atoms of each type. The simulation was initially equilibrated at 250 K for 1 ns within the Number, Volume and Temperature ensemble, during which the ice layer was kept fixed to prevent melting. After equilibration, the position restraints on the ice were removed; the production simulations were carried out under Number, Pressure and Temperature ensemble, that is, at 270 K and 1 atm. The LJ component of the potential was truncated at 0.85 nm, and the long-range electrostatic interactions were managed using the particle–particle particle–mesh algorithm. The temperature is kept constant by Nosé–Hoover thermostat[69] with a relaxation time of 0.1 ps, and pressure is maintained at 1 atm by a Nosé–Hoover barostat with relaxation times of 1 ps. During simulations, the equation for the motion of atoms were integrated using the velocity–Verlet algorithm with a time step of 10 fs. All the visualizations are performed by OVITO[70]. The CHILL+ algorithm was used to distinguish ice molecule from liquid water molecule[71].

The WCP was used to quantify the short-range ordering in the first-nearest neighbour shell[72], $WCP_{mn} = 1 - \frac{Z_{mn}}{\chi_n Z_m}$, where Z_{mn} is the number of n-type atoms around m-type atoms, Z_m is the total number of atoms around m-type atoms, and $\chi_n = 0.2$, is the atomic fraction of n-type atoms in the HEA. The entropy of mixing (ΔS_{mix}) was calculated using the equation $\Delta S_{mix} = -R\sum_{i=1}^{n} x_i \ln x_i$, where R is the gas constant, x_i is the atomic fraction of the ith atom type, and n denotes the number of atom types in the cluster[73].

To validate the robustness of the water and metal interaction models, we performed comparative simulations in which water was described using the all-atom TIP4P/Ice model[53] and metal–metal interactions were treated with the embedded atom method potential[55]

(Supplementary Fig. 16). This simulation was performed using the LAMMPS package. The interactions between water oxygen atoms and metal atoms were modelled using LJ potential, consistent with the approach adopted in Fig. 3. The simulations were carried out in the Number, Pressure and Temperature ensemble at 260 K and 1 atm, with a time step of 2 fs. The dimensions of the simulation box were $5.5 \times 5.5 \times 9.0$ nm^3. A total of 7,540 water molecules and 100 metal atoms were included in the system. The metal atoms consisted of five species—Ag, Au, Cu, Ni and Pt—with 20 atoms of each type. To evaluate the sensitivity of our simulation results to the strength of water–metal interactions, we systematically varied the LJ parameter ε_{MO}, which defines the interaction strength between metal atoms and water molecules. All other simulation parameters, including water and metal models, were identical to those described in Fig. 3. As shown in Supplementary Fig. 17, the formations of large, stable HEA particles were consistently observed across the range $\varepsilon_{MO} = 0.25$–1.0 kcal mol^{-1}.

Single ice crystal characterization by nanolitre osmometer

The growth of single ice crystals was monitored by an Otago Nanolitre Osmometer (Otago Osmometers) with a precision of 0.01 °C. The testing system and procedure have been described in previous literature[74]. To observe the growth of single ice crystals, a submicrolitre volume of metal NP sol was injected into a temperature-controlled sample holder full of silicone oil. The solution immersed in oil was quickly frozen and then slowly warmed to its melting temperature. Once a small (~15 – 20 µm in diameter) single ice crystal appeared, it was maintained for 20 s and the temperature was recorded as the melting temperature (T_m). Then the temperature was lowered to a desired value (T_d). This procedure was captured using a high-speed camera (Phantom V7.3). Supercooling temperature (ΔT) was obtained by $\Delta T = T_m - T_d$. The experiment was repeated at least three times for each ΔT. The growth rate was determined from the recorded images by dividing the elongation by the time elapsed during the growth course, and a mean value was calculated from the repeated experimental videos.

Cryogenic laser confocal microscopy

To confirm the formation of large assemblies and perhaps gels at the ice–water interfaces, a specialized cryogenic laser confocal microscopy was established to capture the process. The apparatus consisted of a Nikon Ti2 Eclipse microscope with a 20× air objective and a 3i Spinning Disk Confocal system. For freezing experiments, a cooling stage was custom-designed, incorporating two Peltier elements (ET-127-10-13) to provide adjustable linear temperature gradients. The freezing cell consisted of two glass microscope slides, bonded together with spacers. Glass slides were thoroughly washed with acetone followed by deionized water and dried with compressed air before each experiment. To visualize the assembly process under fluorescence-field mode, we prepared a solution by mixing PtAuAgCuIn NP sol (0.2 mM, 0.5 ml) with TVP solution (0.05 mg ml^{-1}, 0.5 ml) to obtain an AIEgen-modified metal NP solution. This solution was illuminated using a 480 nm laser to image the fluorescent tracer particles. We applied 30 µl of the mixture to one side of the freezing cell to ensure full surface coverage and precooled it at 278 K for 10 min. We then established a temperature gradient by setting the temperature on one side to 268 K, initiating ice growth until the ice–water interface reached an equilibrium position. As cooling continued on this side, the ice front advanced slowly at a rate of 1 µm s^{-1}. During this process, we recorded the aggregation of particles at the growth front of the moving ice crystals under fluorescence-field mode, capturing dynamic changes in the assembly.

Electron tomography acquisition

Fused multimodal electron tomography of Au@PtAgCuInPdRhRuCoBiNi aerogel was carried out employing a Thermo Fisher Scientific Spectra Ultra S/TEM equipped with a new generation Ultra-X EDX detector. Specifically, HAADF and EDX tilt series were simultaneously acquired at 300 kV, with a screen current of 50 pA and convergence semi-angle of 18.0 mrad. ADF-STEM images were collected from −52.5° to 52.5°, with a 2.5° angular increment. To minimize drift at each tilt angle, three consecutive images were acquired per angle with a 3-µs dwell time. Simultaneous collection of EDX spectrums was performed at the angle spanning from −50° to +50°, with a 10° angular increment and a dwell time of 10 µs for 125 frames. The total electron dose was estimated to be 2.32×10^5 e Å^{-2} for ADF-STEM and EDX. To assess any structural changes during data acquisition, we compared the images taken at zero degrees before, during and after the tilt series acquisition and found no substantial structural changes.

Image pre-processing

A normalized cross-correlation was applied in drift correction and registration of three consecutive images at each tilt angle to correct sample drift and distortion during ADF-STEM acquisition. The images were then averaged to improve the signal-to-noise ratio. Subsequently, a block matching and three-dimensional filtering (BM3D) algorithm, proven effective for AET data, was employed for images denoising[75–78]. The denoised images, including the ADF projections from EDX measures, were processed using the Otsu threshold to compute the two-dimensional masks of the object, and the background was estimated via a Laplacian interpolation[79]. Meanwhile, the masks generated from the ADF images were utilized to subtract the background signals of the raw mapping in EDX at the identical angle. After background subtraction, the ADF images were aligned through centre of mass and common line methods to further minimize errors of the tilt series[80]. The drift and rotation parameters obtained from the alignment of ADF projections of EDX were subsequently applied to the chemical mapping to achieve precise alignment.

Fused multimodal electron tomography

A fused multimodal electron tomography was employed to recover the three-dimensional chemical and structural distribution from the aligned ADF and EDX tilt series[61]. Specifically, this reconstruction process was guided by minimizing a cost function that accounts for the elastic and inelastic scattering measurements. The cost function was expressed as

$$\hat{\mathbf{x}} = \mathrm{argmin}_{\mathbf{x}\geq 0} \lambda_1 \Psi_1(\mathbf{x}) + \lambda_2 \Psi_2(\mathbf{x}) + \lambda_3 \Psi_3(\mathbf{x}).$$

Here, $\hat{\mathbf{x}}$ represents the final three-dimensional chemical reconstruction, and λ are regularization parameters that control the relative importance of each term in the optimization. $\Psi_1(\mathbf{x})$ is the fidelity term for the HAADF data, ensuring that the reconstruction aligns with the measured HAADF projections. $\Psi_2(\mathbf{x})$ is the fidelity term for the chemical data from EDX, ensuring that the reconstructed chemical distribution matches the measured chemical mapping images. $\Psi_3(\mathbf{x})$ is isotropic total variation (TV) regularization, enforcing a sparse gradient magnitude to reduce noise and preserve sharp boundaries between different chemical volumes.

$$\Psi_1(\mathbf{x}) = \frac{1}{2} \left\| \mathbf{A}_h \sum_i (Z_i \mathbf{x}_i)^\gamma - \mathbf{b}_H \right\|_2^2$$

$$\Psi_2(\mathbf{x}) = \sum_i (\mathbf{1}^T \mathbf{A}_c \mathbf{x}_i - \mathbf{b}_i^T \log(\mathbf{A}_c \mathbf{x}_i + \varepsilon))$$

$$\Psi_3(\mathbf{x}) = \sum_i ||\mathbf{x}_i||_{TV}$$

Here $\mathbf{x}_i$ is reconstructed three-dimensional elemental distributions of element i, $\mathbf{b}_H$ is the experimental ADF projections, $\mathbf{b}_i$ is the experimental EDX image for element i, and $\mathbf{A}_h$ and $\mathbf{A}_c$ are forward projection

matrices for ADF and chemical modalities. The optimization procedure proceeded via the combination of iterative gradient descent for the first two parts and then assess TV proximal operator for denoising and refining both the structural and chemical components of the specimen until convergence was achieved, which ensures that the chemical distributions maintained realistic, physically meaningful values. The convergence was monitored by examining the smooth decay of each term in the cost function, particularly focusing on the reduction in the residuals of the fidelity terms. A smooth and asymptotic reduction in all terms ensures reliable reconstruction, and regularization parameters (λ) are optimized through analysis of the Pareto front. The Avizo platform was used to render the final three-dimensional multimodal reconstruction volumes.

Data availability

The data that support the findings of this study are available via Zenodo at https://doi.org/10.5281/zenodo.17129735 (ref. 81).

Code availability

The source codes for the fused multimodal electron tomography of this work are available via GitHub at https://github.com/yang-lab-westlake-u/HEA-ice-fused-tomo.

References

1. Cantor, B., Chang, I. T. H., Knight, P. & Vincent, A. J. B. Microstructural development in equiatomic multicomponent alloys. *Mater. Sci. Eng. A* **375**, 213–218 (2004).
2. Yeh, J.-W. et al. Nanostructured high-entropy alloys with multiple principal elements: novel alloy design concepts and outcomes. *Adv. Eng. Mater.* **6**, 299–303 (2004).
3. Rao, Z. et al. Machine learning-enabled high-entropy alloy discovery. *Science* **378**, 78–85 (2022).
4. Li, Z., Pradeep, K., Deng, Y., Raabe, D. & Tasan, C. Metastable high-entropy dual-phase alloys overcome the strength–ductility trade-off. *Nature* **534**, 227–230 (2016).
5. Ding, Q. et al. Tuning element distribution, structure and properties by composition in high-entropy alloys. *Nature* **574**, 223–227 (2019).
6. Dirksen, J. A. & Ring, T. A. Fundamentals of crystallization: kinetic effects on particle size distributions and morphology. *Chem. Eng. Sci.* **46**, 2389–2427 (1991).
7. Cushing, B., Kolesnichenko, V. & O'Conno, C. Recent advances in the liquid-phase syntheses of inorganic nanoparticles. *Chem. Rev.* **104**, 3893–3946 (2004).
8. Dey, G. et al. Chemical insights into the formation of colloidal high entropy alloy nanoparticles. *ACS Nano* **17**, 5943–5955 (2023).
9. Chen, J. & Shao, L. Mass production of nanoparticles by high gravity reactive precipitation technology with low cost. *China Part.* **1**, 64–69 (2003).
10. Yao, Y. et al. Carbothermal shock synthesis of high-entropy-alloy nanoparticles. *Science* **359**, 1489–1494 (2018).
11. Kim, K. S. et al. Continuous synthesis of high-entropy alloy nanoparticles by in-flight alloying of elemental metals. *Nat. Commun.* **15**, 1450 (2024).
12. Yao, Y. et al. High-entropy nanoparticles: synthesis–structure–property relationships and data-driven discovery. *Science* **376**, eabn3103 (2022).
13. Gao, S. et al. Synthesis of high-entropy alloy nanoparticles on supports by the fast moving bed pyrolysis. *Nat. Commun.* **11**, 2016 (2020).
14. Wu, D. et al. Platinum-group-metal high-entropy-alloy nanoparticles. *J. Am. Chem. Soc.* **142**, 13833–13838 (2020).
15. Broge, N. et al. Autocatalytic formation of high-entropy alloy nanoparticles. *Angew. Chem. Int. Ed.* **59**, 21920–21924 (2020).
16. Cao, G. et al. Liquid metal for high-entropy alloy nanoparticles synthesis. *Nature* **619**, 73–77 (2023).
17. Stibal, M., Sabacka, M. & Zarsky, J. Biological processes on glacier and ice sheet surfaces. *Nature Geosci.* **5**, 771–774 (2012).
18. Attwater, J., Wochner, A., Pinheiro, V. B., Coulson, A. & Holliger, P. Ice as a protocellular medium for RNA replication. *Nat. Commun.* **1**, 76 (2010).
19. Cebeci, T. & Kafyeke, F. Aircraft icing. *Annu. Rev. Fluid Mech.* **35**, 11–21 (2003).
20. Slater, B. & Michaelides, A. Surface premelting of water ice. *Nat. Rev. Chem.* **3**, 172–188 (2019).
21. Moore, E. & Molinero, V. Structural transformation in supercooled water controls the crystallization rate of ice. *Nature* **479**, 506–508 (2011).
22. Backhouse, T. W. The formation of ice. *Nature* **39**, 437 (1889).
23. Peng, J. et al. The effect of hydration number on the interfacial transport of sodium ions. *Nature* **557**, 701–705 (2018).
24. Hong, J. et al. Imaging surface structure and premelting of ice Ih with atomic resolution. *Nature* **630**, 375–380 (2024).
25. Li, H. et al. High-entropy alloy aerogels: a new platform for carbon dioxide reduction. *Adv. Mater.* **35**, 2209242 (2023).
26. Deville, S. et al. Freezing as a path to build complex composites. *Science* **311**, 515–518 (2006).
27. Cheng, Q. & Jiang, L. Mimicking nacre by ice templating. *Angew. Chem. Int. Ed.* **56**, 934–935 (2017).
28. Fan, Q. et al. Precise control over kinetics of molecular assembly: production of particles with tunable sizes and crystalline forms. *Angew. Chem. Int. Ed.* **59**, 15141–15146 (2020).
29. Wu, S. et al. Ion-specific ice recrystallization provides a facile approach for the fabrication of porous materials. *Nat. Commun.* **8**, 15154 (2017).
30. Wu, M. et al. Biomimetic, knittable aerogel fiber for thermal insulation textile. *Science* **382**, 1379–1383 (2023).
31. Zhao, S. et al. Biopolymer aerogels and foams: chemistry, properties, and applications. *Angew. Chem. Int. Ed.* **57**, 7580–7608 (2018).
32. Si, Y. et al. Ultralight and fire-resistant ceramic nanofibrous aerogels with temperature-invariant superelasticity. *Sci. Adv.* **4**, eaas8925 (2018).
33. Gao, H. et al. Super-elastic and fatigue resistant carbon material with lamellar multi-arch microstructure. *Nat. Commun.* **7**, 12920 (2016).
34. Zhang, P. et al. A microstructured graphene/poly(*N*-isopropylacrylamide) membrane for intelligent solar water evaporation. *Angew. Chem. Int. Ed.* **57**, 16343–16347 (2018).
35. Song, P., Qin, H., Gao, H., Cong, H. & Yu, S. Self-healing and superstretchable conductors from hierarchical nanowire assemblies. *Nat. Commun.* **9**, 2786 (2018).
36. Halloran, J. Making better ceramic composites with ice. *Science* **311**, 479–480 (2006).
37. Mayer, E. New method for vitrifying water and other liquids by rapid cooling of their aerosols. *J. Appl. Phys.* **58**, 663–667 (1985).
38. Jones, H. Splat cooling and metastable phases. *Rep. Prog. Phys.* **36**, 1425 (1973).
39. Mayer, E. Vitrification of pure liquid water. *J. Microsc.* **140**, 3–15 (1985).
40. Wei, H. et al. Iced photochemical reduction to synthesize atomically dispersed metals by suppressing nanocrystal growth. *Nat. Commun.* **8**, 1490 (2017).
41. Wei, H. et al. Ice melting to release reactants in solution syntheses. *Angew. Chem. Int. Ed.* **57**, 3354–3359 (2018).
42. Du, R. et al. Freeze–thaw-promoted fabrication of clean and hierarchically structured noble-metal aerogels for electrocatalysis and photoelectrocatalysis. *Angew. Chem. Int. Ed.* **59**, 8293–8300 (2020).

43. Du, R. et al. Specific ion effects directed noble metal aerogels: versatile manipulation for electrocatalysis and beyond. *Sci. Adv.* **5**, eaaw4590 (2019).
44. Xie, P. et al. Highly efficient decomposition of ammonia using high-entropy alloy catalysts. *Nat. Commun.* **10**, 4011 (2019).
45. Batchelor, T. A. A. et al. High-entropy alloys as a discovery platform for electrocatalysis. *Joule* **3**, 834–845 (2019).
46. Sun, Y. & Dai, S. High-entropy materials for catalysis: a new frontier. *Sci. Adv.* **7**, eabg1600 (2021).
47. Sarkar, A. et al. High entropy oxides for reversible energy storage. *Nat. Commun.* **9**, 3400 (2018).
48. Koželj, P. et al. Discovery of a superconducting high-entropy alloy. *Phys. Rev. Lett.* **113**, 107001 (2014).
49. Ai, Y. et al. Ultra-small high-entropy alloy nanoparticles: efficient nanozyme for enhancing tumor photothermal therapy. *Adv. Mater.* **35**, 2302335 (2023).
50. Chang, L. et al. High-entropy materials for prospective biomedical applications: challenges and opportunities. *Adv. Sci.* **11**, 2406521 (2024).
51. Yao, Y. et al. Extreme mixing in nanoscale transition metal alloys. *Matter* **4**, 2340–2353 (2021).
52. Chen, S. et al. Simultaneously enhancing the ultimate strength and ductility of high-entropy alloys via short-range ordering. *Nat. Commun.* **12**, 4953 (2021).
53. Abascal, J. L. F., Sanz, E., García Fernández, R. & Vega, C. A potential model for the study of ices and amorphous water: TIP4P/Ice. *J. Chem. Phys.* **122**, 234511 (2005).
54. Molinero, V. & Moore, E. B. Water modeled as an intermediate element between carbon and silicon. *J. Phys. Chem. B* **113**, 4008–4016 (2009).
55. Zhou, X. W., Johnson, R. A. & Wadley, H. N. G. Misfit-energy-increasing dislocations in vapor-deposited CoFe/NiFe multilayers. *Phys. Rev. B* **69**, 144113 (2004).
56. Dedovets, D., Monteux, C. & Deville, S. Five-dimensional imaging of freezing emulsions with solute effects. *Science* **360**, 303–306 (2018).
57. Graether, S. et al. β-Helix structure and ice-binding properties of a hyperactive antifreeze protein from an insect. *Nature* **406**, 325–328 (2000).
58. He, Z., Liu, K. & Wang, J. Bioinspired materials for controlling ice nucleation, growth, and recrystallization. *Acc. Chem. Res.* **51**, 1082–1091 (2018).
59. Biggs, C. I. et al. Polymer mimics of biomacromolecular antifreezes. *Nat. Commun.* **8**, 1546 (2017).
60. Weng, B. et al. Controlled synthesis of noble metal aerogels mediated by salts. *Nat. Protoc.* https://doi.org/10.1038/s41596-025-01185-1 (2025).
61. Schwartz, J. et al. Imaging 3D chemistry at 1 nm resolution with fused multi-modal electron tomography. *Nat. Commun.* **15**, 3555 (2024).
62. Wu, C. et al. A catalyst family of high-entropy alloy atomic layers with square atomic arrangements comprising iron- and platinum-group metals. *Sci. Adv.* **10**, eadl3693 (2024).
63. Zhao, X. et al. Multiple metal–nitrogen bonds synergistically boosting the activity and durability of high-entropy alloy electrocatalysts. *J. Am. Chem. Soc.* **146**, 3010–3022 (2024).
64. Plimpton, S. Fast parallel algorithms for short-range molecular-dynamics. *J. Comput. Phys.* **117**, 1–19 (1995).
65. Heinz, H., Vaia, R. A., Farmer, B. L. & Naik, R. R. Accurate simulation of surfaces and interfaces of face-centered cubic metals using 12-6 and 9-6 Lennard–Jones potentials. *J. Phys. Chem. C* **112**, 17281–17290 (2008).
66. Lupi, L., Hudait, A. & Molinero, V. Heterogeneous nucleation of ice on carbon surfaces. *J. Am. Chem. Soc.* **136**, 3156–3164 (2014).
67. Somlyai-Sipos, L. & Baumli, P. Wettability of metals by water. *Metals* **12**, 1274 (2022).
68. Matsumoto, M., Yagasaki, T. & Tanaka, H. GenIce: hydrogen-disordered ice generator. *J. Comput. Chem.* **39**, 61–64 (2018).
69. Nosé, S. A molecular-dynamics method for simulations in the canonical ensemble. *Mol. Phys.* **52**, 255–268 (1984).
70. Stukowski, A. Visualization and analysis of atomistic simulation data with OVITO-the open visualization tool. *Model. Simul. Mater. Sci. Eng.* **18**, 015012 (2010).
71. Nguyen, A. H. & Molinero, V. Identification of clathrate hydrates, hexagonal ice, cubic ice, and liquid water in simulations: the CHILL+ algorithm. *J. Phys. Chem. B* **119**, 9369–9376 (2015).
72. Cowley, J. M. X-ray measurement of order in single crystals of Cu_3Au. *J. Appl. Phys.* **21**, 24–30 (1950).
73. Liu, Y. H. et al. Toward controllable and predictable synthesis of high-entropy alloy nanocrystals. *Sci. Adv.* **9**, eadf9931 (2023).
74. Bai, G. et al. Oxidized quasi-carbon nitride quantum dots inhibit ice growth. *Adv. Mater.* **29**, 1606843 (2017).
75. Dabov, K., Foi, A., Katkovnik, V. & Egiazarian, K. Image denoising by sparse 3-D transform-domain collaborative filtering. *IEEE Trans. Image Process.* **16**, 2080–2095 (2007).
76. Yang, Y. et al. Determining the three-dimensional atomic structure of an amorphous solid. *Nature* **592**, 60–64 (2021).
77. Moniri, S. et al. Three-dimensional atomic structure and local chemical order of medium- and high-entropy nanoalloys. *Nature* **624**, 564–569 (2023).
78. Yang, Y. et al. Atomic-scale identification of active sites of oxygen reduction nanocatalysts. *Nat. Catal.* **7**, 796–806 (2024).
79. Otsu, N. A. Threshold selection method from gray-level histograms. *IEEE Trans. Syst. Man Cybern.* **9**, 62–66 (1979).
80. Chen, C.-C. et al. Three-dimensional imaging of dislocations in a nanoparticle at atomic resolution. *Nature* **496**, 74–77 (2013).
81. Xu, T. & Yang, Y. Synthesising high-entropy alloy nanoparticles, aerogels and coatings using a bilayer ice recrystallization method (scientific article published in *Nature Synthesis*, 2025). *Zenodo* https://doi.org/10.5281/zenodo.17129735 (2025).

Acknowledgements

This work is primarily supported by the National Natural Science Foundation of China Joint Fund for Regional Innovation and Development (grant no. U24A20495) by Z.H. Z.H. also acknowledges the support by National Natural Science Foundation of China (grant no. 22122206). Y.Y. was supported by National Natural Science Foundation of China (grant no. 52473240). R.D. was supported by National Natural Science Foundation of China (grant nos. 22202009, 22572008), Beijing Natural Science Foundation (grant no. 2232063) and Hebei Natural Science Foundation (grant no. B2024105005). Xiaoting Chen, D.W. and Xiaofei Chen acknowledge the support by National Natural Science Foundation of China (grant nos. 22302011, 12304098 and 23CAA01015). C.Z. acknowledges the support by Youth Innovation Program of Universities in Shandong Province (grant no. 2021KJ091). We thank Y. Xu at Beihang University for assistance with the test of in situ cryogenic laser confocal microscopy, R. Cai at Analysis and Testing Center, Beijing Institute of Technology and Q. Jiang at Instrumentation and Service Center for Physical Science, Westlake University for assistance with TEM measurements.

Author contributions

Z.H., R.D. and Y.Y. conceived the idea, designed the experiments and supervised the research project. K.L., X.S., Q.W. and Xiaoting Chen conducted the BLIR experiments. K.L., Q.W., S.G. and T.X. performed cryogenic TEM, fused chemical electron tomography experiments and tomographic reconstruction. C.Z. and D.W. conducted the simulations. K.L., X.S., Q.W., Xiaofei Chen and Xiaoting Chen analysed the data.

Z.H., R.D. and Y.Y. wrote the study. All authors contributed to the experiments and discussion of the paper.

Competing interests
The authors declare no competing interests.

Additional information
Extended data is available for this paper at https://doi.org/10.1038/s44160-025-00931-3.

Supplementary information The online version contains supplementary material available at https://doi.org/10.1038/s44160-025-00931-3.

Correspondence and requests for materials should be addressed to Ran Du, Yao Yang or Zhiyuan He.

Peer review information *Nature Synthesis* thanks Bharat Gwalani, Mauricio Ponga and the other, anonymous, reviewer(s) for their contribution to the peer review of this work. Primary Handling Editor: Peter Seavill, in collaboration with the *Nature Synthesis* team.

https://doi.org/10.1038/s44160-025-00931-3

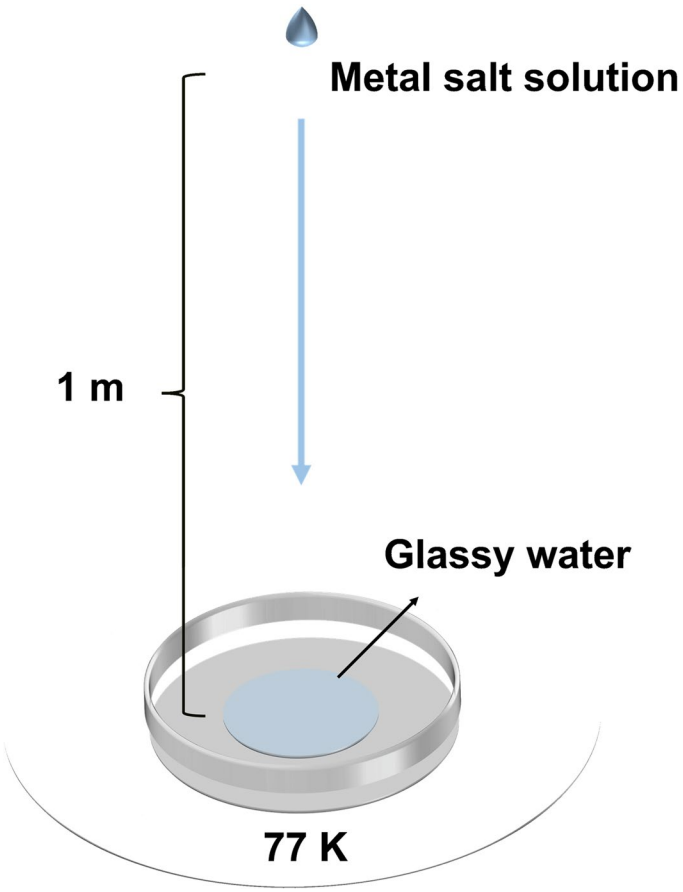

Extended Data Fig. 1 | Schematic diagram of the splat-cooling process. A thin layer of glassy water was formed at the cold stage, the droplet of metal salt solution was dropped from 1 m height for splat cooling.

https://doi.org/10.1038/s44160-025-00931-3

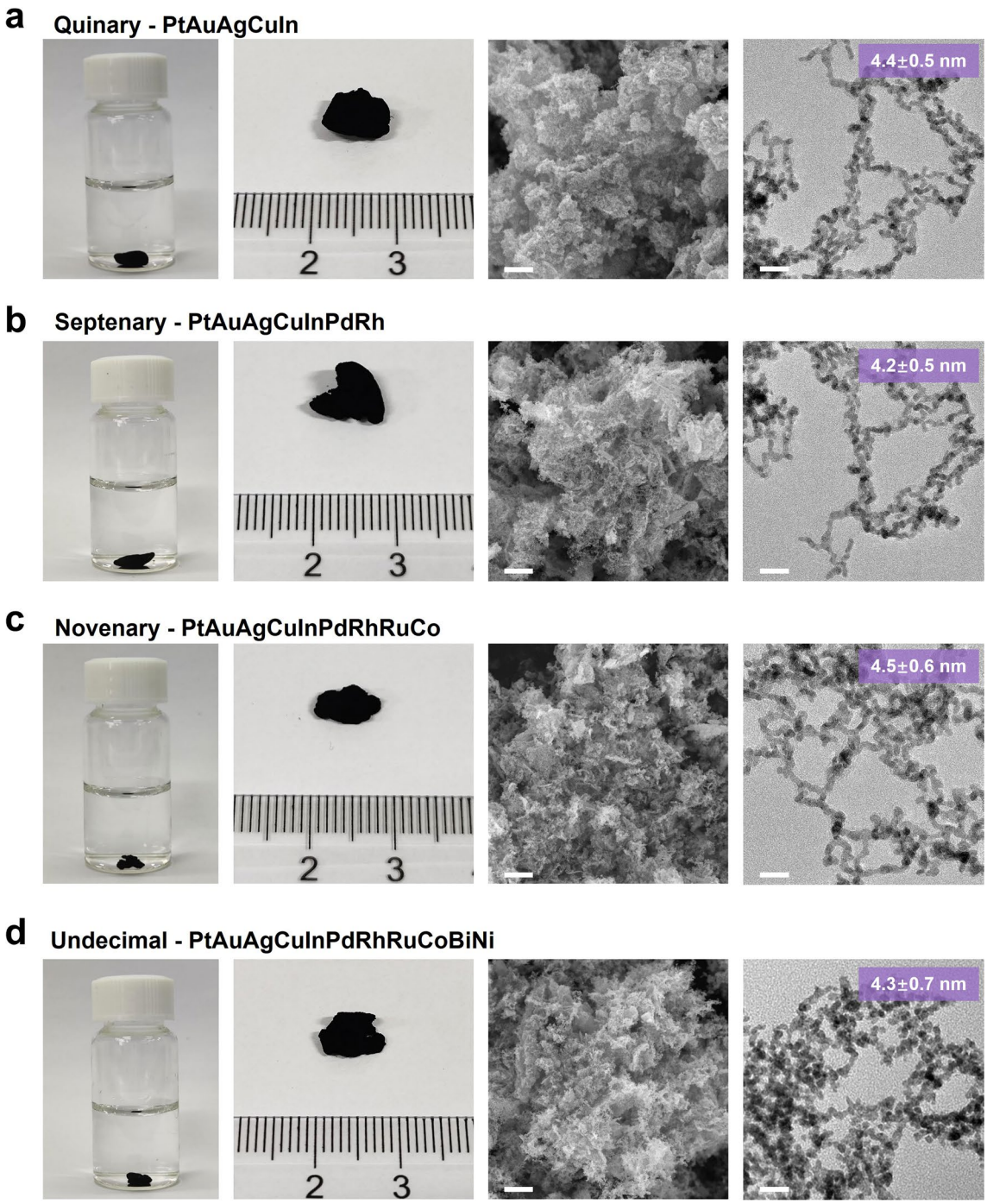

Extended Data Fig. 2 | Characterization of the morphology of diverse self-standing HEAAs at the macroscopic and microscopic level. Optical images, SEM images, and TEM images of (**a**) quinary PtAuAgCuIn gels, (**b**) septenary PtAuAgCuInPdRh gels, (**c**) novenary PtAuAgCuInPdRhRuCo gels, (**d**) undecimal PtAuAgCuInPdRhRuCoBiNi gels. Optical images scaled by rulers. Scale bar for SEM, 1 μm. Scale bar for TEM, 20 nm.

https://doi.org/10.1038/s44160-025-00931-3

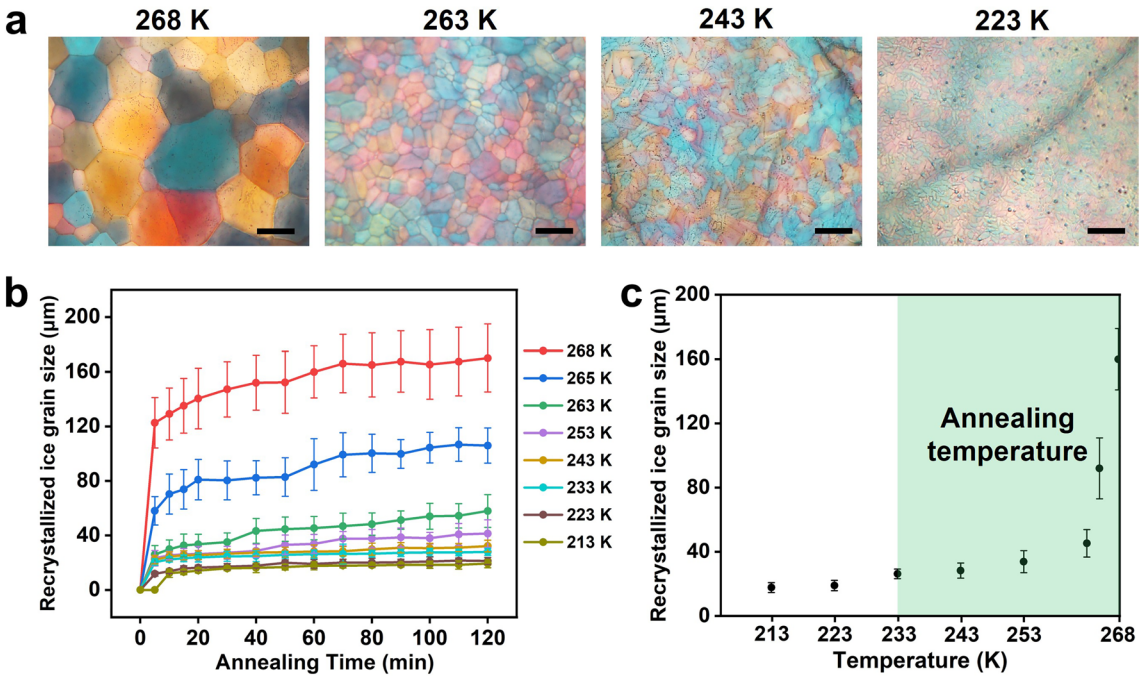

Extended Data Fig. 3 | Analysis of recrystallization temperature. a, Polarized optical microscopy images of ice recrystallization at various temperatures after 60 minutes. **b**, The mean size of the ice grains recrystallized at different annealing times under different temperatures. For each recrystallization temperature, 25 grains are selected for each annealing time point. The error bars show the standard deviation of mean values. **c**, The mean size of the ice grains recrystallized at various temperatures after 60 minutes. For each recrystallization temperature, 25 grains are selected. The error bars show the standard deviation of mean values. Scale bar, 100 μm.

https://doi.org/10.1038/s44160-025-00931-3

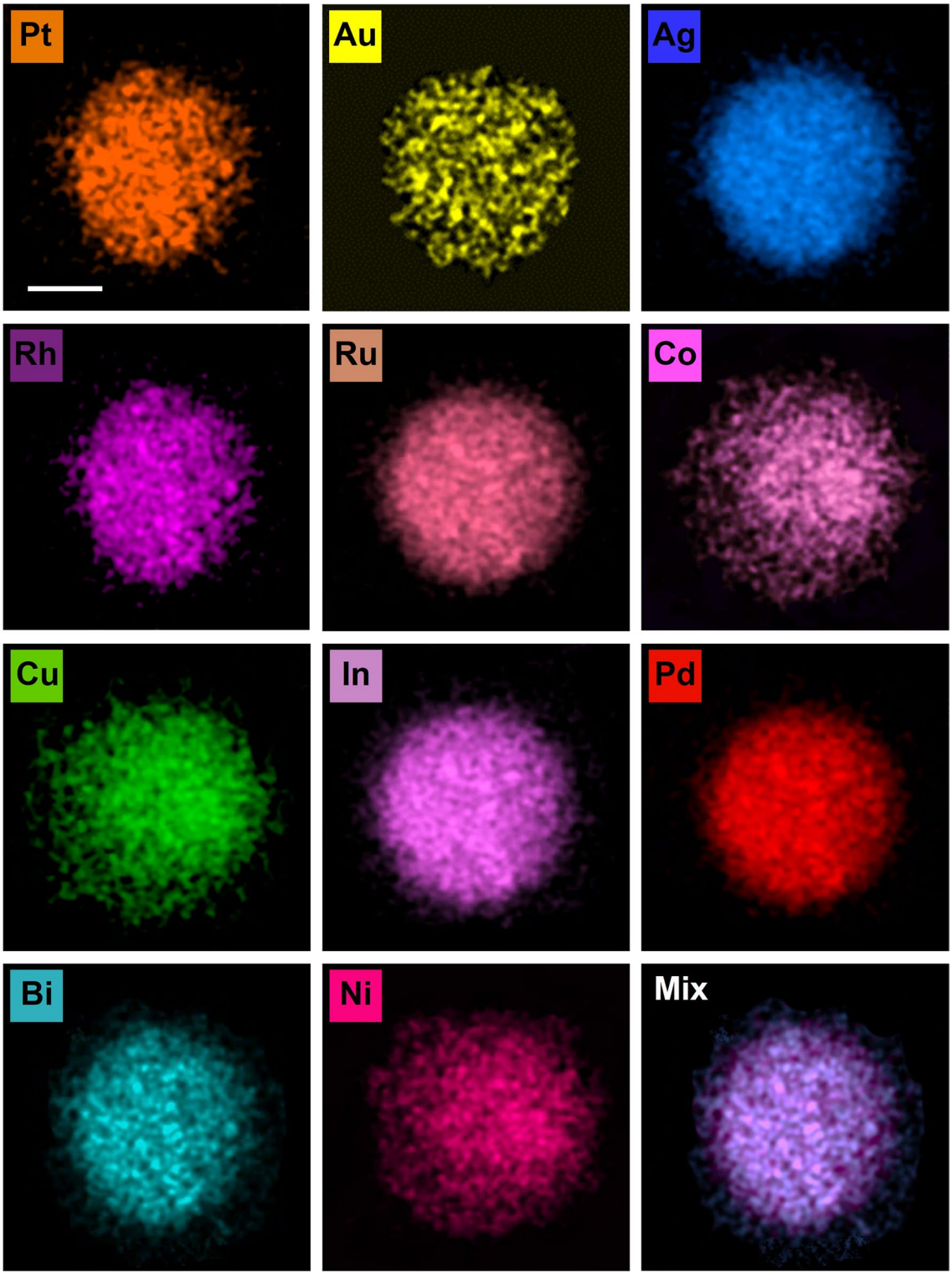

Extended Data Fig. 4 | STEM-EDX maps of an undecimal PtAuAgCuInPdRhRuCoBiNi HEA NP. The element mapping of a HEA NP with 11 elements, which show a uniform distribution. Scale bar, 2 nm.

https://doi.org/10.1038/s44160-025-00931-3

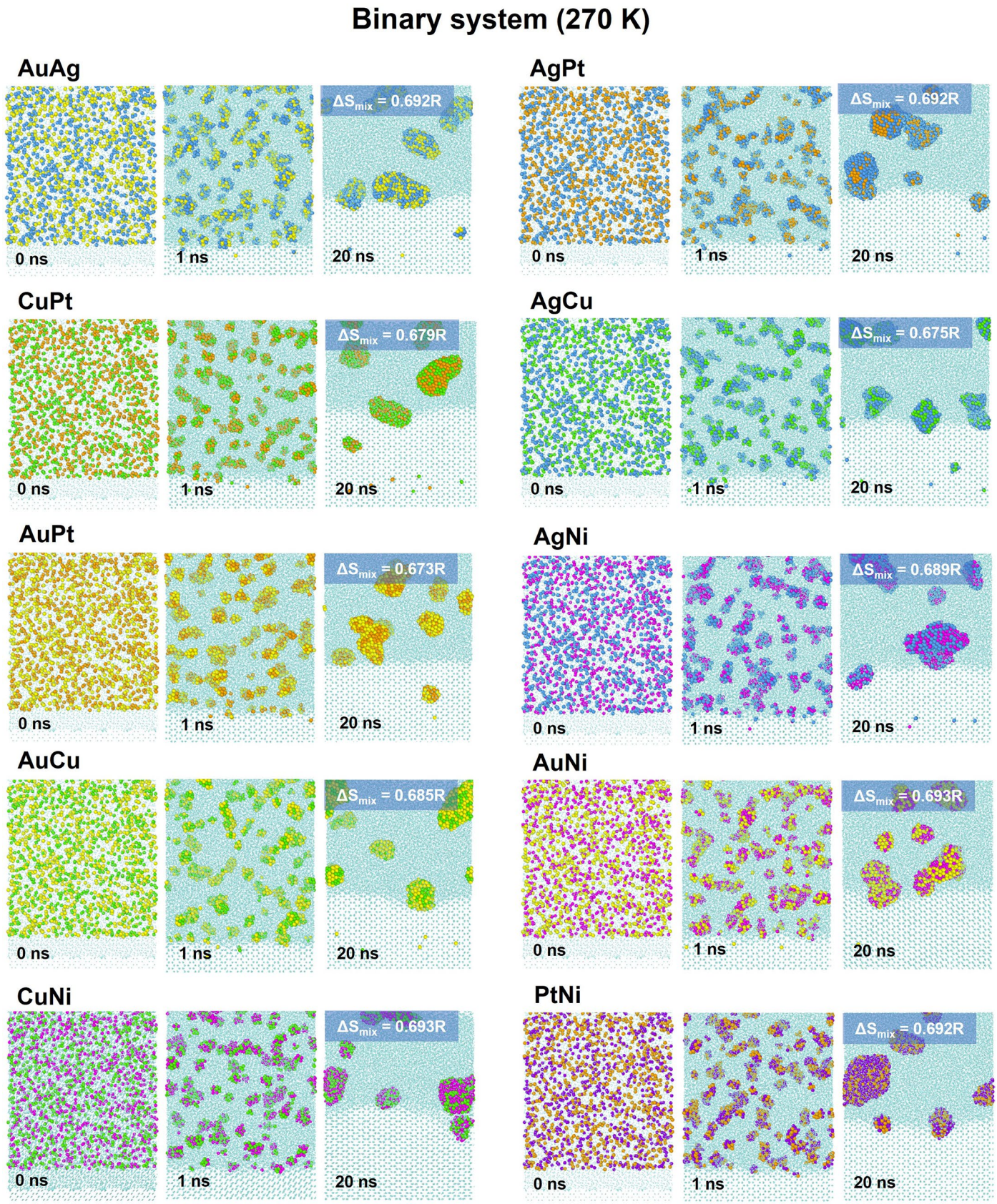

Extended Data Fig. 5 | Snapshots of the MD simulations for indicated binary systems. The atomic arrangement of 10 bimetallic systems (AuAg, AgPt, CuPt, AgCu, AuPt, AgNi, AuCu, AuNi, CuNi, PtNi) at 0, 1 and 20 ns. All of them formed clusters with uniform element distributions. The corresponding mix entropy is shown in the right corner.

https://doi.org/10.1038/s44160-025-00931-3

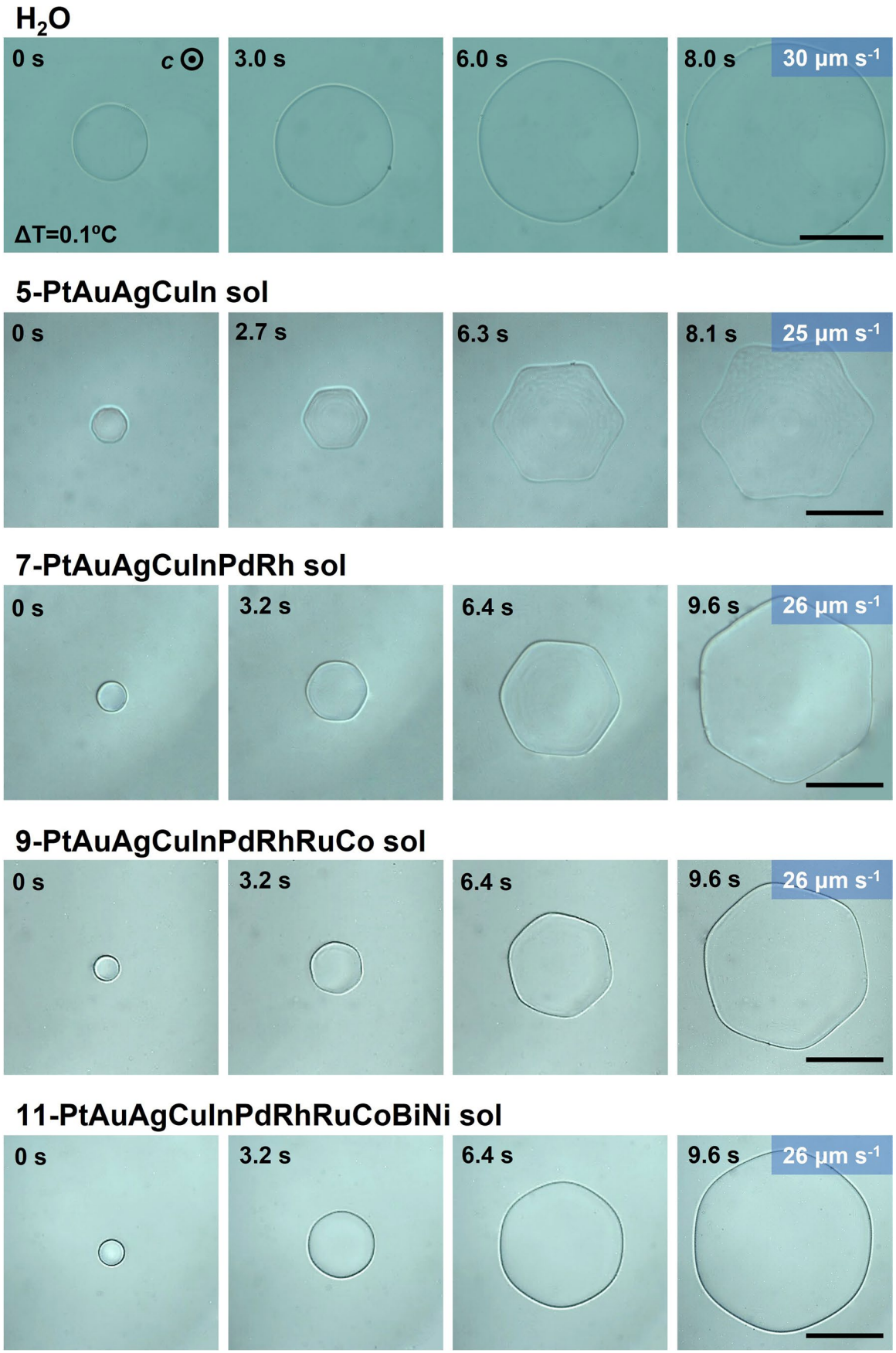

Extended Data Fig. 6 | Growth processes of single ice crystals in pure water and different metal NP sols. The optical microscopic images of crystallization of single ice crystal by pure water and sol with 5, 7, 9 and 11 metal elements. ΔT = 0.1 °C, c_M = 0.2 mM. Scale bar, 100 μm.

https://doi.org/10.1038/s44160-025-00931-3

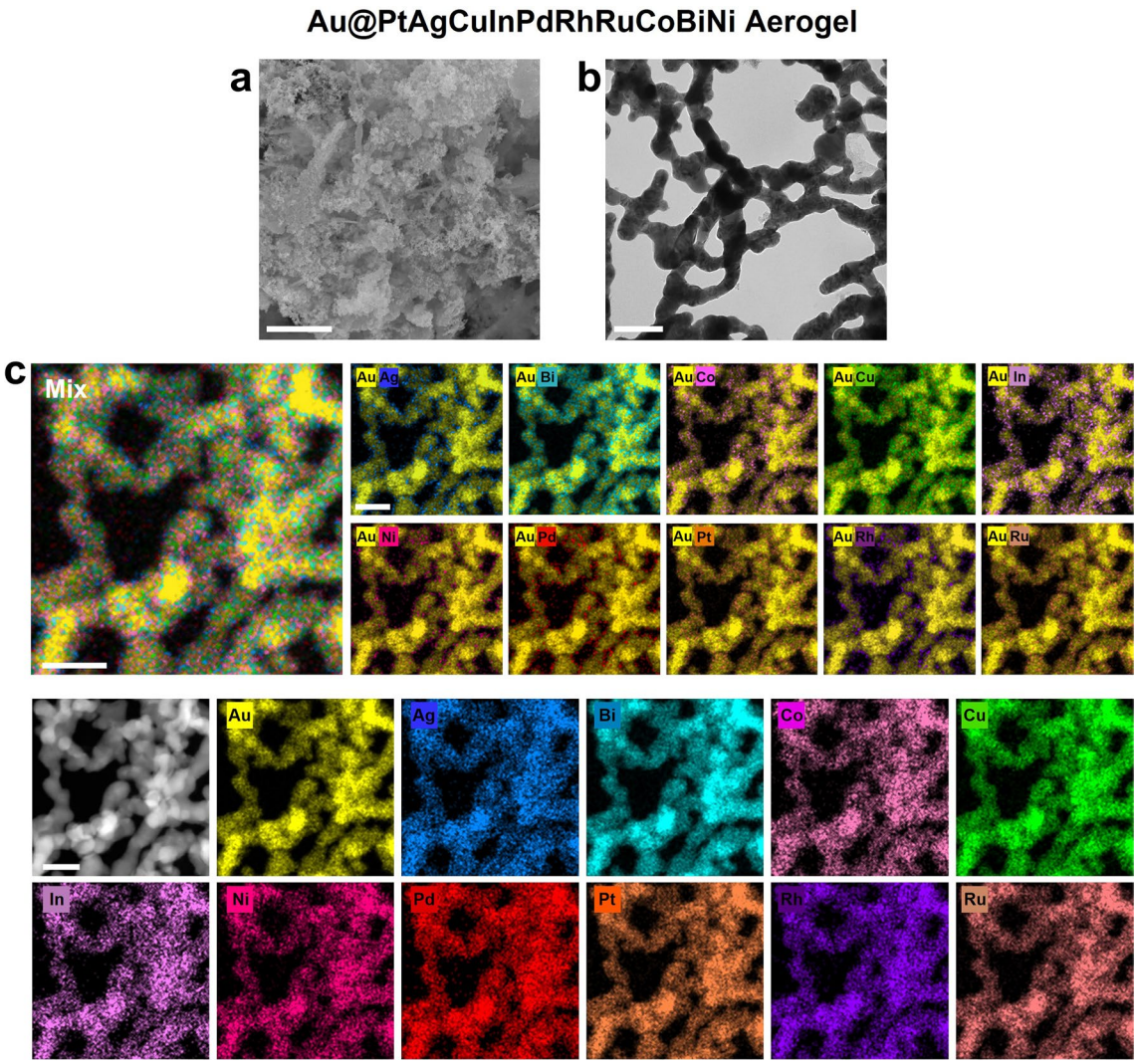

Extended Data Fig. 7 | Electron microscope characterization of Au aerogel with 10-HEA coatings. a, SEM image of the Au@PtAgCuInPdRhRuCoBiNi aerogel. Scale bar, 1 μm. **b**, TEM image of the core-shell aerogel. Scale bar, 100 nm. **c**, EDX elemental mappings of the core-shell aerogel. Scale bar, 50 nm.

https://doi.org/10.1038/s44160-025-00931-3

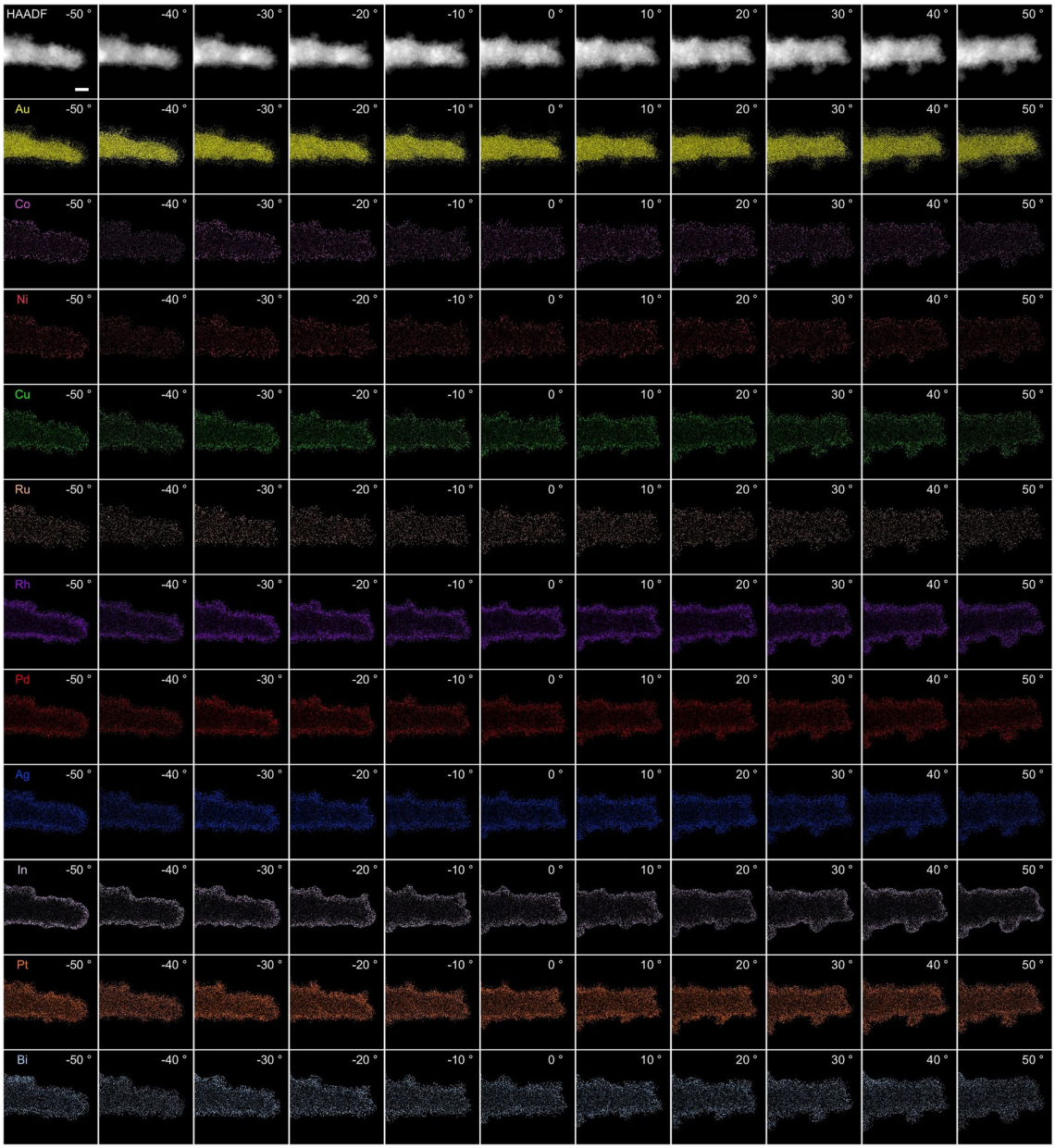

Extended Data Fig. 8 | Tilt series for fused multi-modal electron tomography on Au@PtAgCuInPdRhRuCoBiNi core-shell aerogel. HAADF-STEM and EDX images of a portion of the Au@PtAgCuInPdRhRuCoBiNi core-shell aerogel. The tilting range is from -50° to 50°, the angle step is 10°. Scale bar, 20 nm.

https://doi.org/10.1038/s44160-025-00931-3

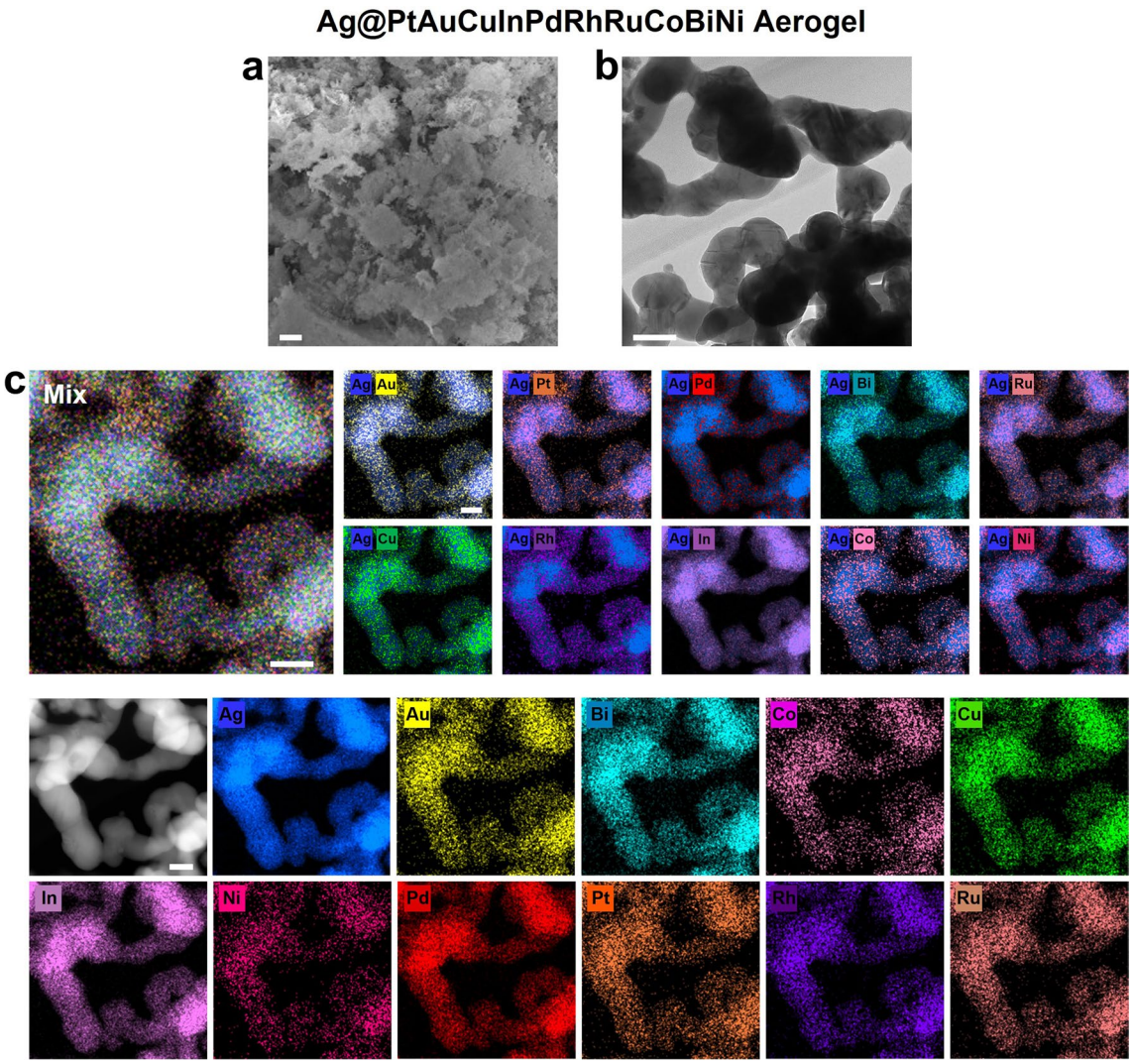

Extended Data Fig. 9 | Electron microscope characterization of Ag aerogel with 10-HEA coatings. a, SEM image of the Ag@PtAuCuInPdRhRuCoBiNi aerogel. Scale bar, 1 µm. **b**, TEM image of the core-shell aerogel. Scale bar, 100 nm. **c**, EDX elemental mappings of the core-shell aerogel. Scale bar, 50 nm.

https://doi.org/10.1038/s44160-025-00931-3

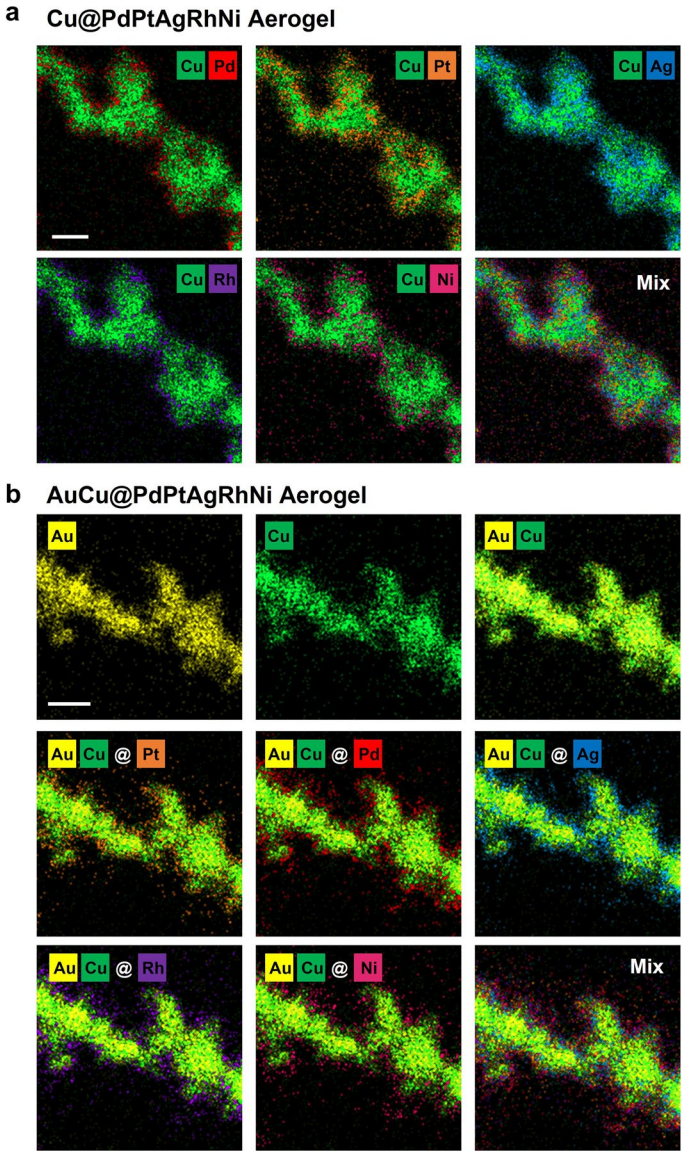

Extended Data Fig. 10 | Electron microscope characterization of metal and alloy aerogel with 5-HEA coatings. a, EDX elemental mappings of Cu@PtPdAgRhNi aerogel. Scale bar, 10 nm. **b**, EDX elemental mappings of AuCu@PtPdAgRhNi aerogel. Scale bar, 10 nm.